

Single-Material, Near-Infrared Selective Absorber Based on Refractive Index-Tunable Tamm Plasmon Structure

So Hee Kim, Joo Hwan Ko, Young Jin Yoo, Min Seok Kim, Gil Ju Lee, Satoshi Ishii, and Young Min Song*

As a powerful planar plasmonics, Tamm plasmon (TP) structures open up new possibilities for high-efficiency photonic applications demanding high quality (Q)-factor with scalability and spectral tunability. Despite the theoretical advantages of TP structures, TP configurations alternately stacked within limited materials and integer ranges result in thicker device sizes and still struggle to achieve ideal designs. Here, by introducing a computational model with varying design parameters, the configurations of high-performance TPs are presented within thin scale. However, the optimized configuration is hard to be realized with limited conventional materials. In this study, the effective refractive index is tailored through porosity change to achieve optimized design parameters, resulting in high Q-factors (≈ 45) and near-unity absorptance ($\approx 99\%$) for sub-micron scale TPs ($\approx 0.7 \mu\text{m}$) based on single material. To verify single-material TPs (SMTPs), the real and imaginary parts of the optical impedances are calculated, which are well matching each other, resulting in unity absorption. Using the designed structure, SMTPs are experimentally fabricated based on glancing angle deposition. As a practical demonstration, SMTPs are combined with a metal–semiconductor–metal photodetector as an ultra-sensitive narrowband photodetector.

efficient photonic applications such as near infrared spectra analysis,^[1] telecommunications,^[2] biomedical and chemical sensing.^[3] Rapidly advancing plasmonics are of particular interest, along with their selective light-trapping with strongly localized photon energy, surface plasmons (SPs) have attracted attention due to their potential applications in medicine and chemistry,^[4,5] as well as optical switching and near-field photonics.^[6–8] However, many studies still rely on the Kretschmann-Raether excitation method,^[9] requiring additional equipment to couple external light to surface modes at high angles of incidence (such as prisms),^[10] or demand a metal/dielectric hybrid systems with delicately designed nanostructures to localize the photon energy in a deep-subwavelength region.^[11] Unlike SPs, Tamm plasmons (TPs) can be directly observed with direct incidence without prism couplers and/or nanostructure. Also, the TPs structure can support surface waves dispersed within the light cone.^[12] Optical TPs can form at the interfaces between distributed Bragg reflectors (DBRs) and with layers having optical thicknesses (t_{opt}) close to half the wavelength of light, similar to the electronic states that can occur in the energy bandgap of a crystal surface.^[13,14] Because of their scalability and spectral tunability with a high quality (Q)-factor, and as sophisticated patterning is not required, TPs can be exploited in high-efficiency photonic applications; e.g., for photodetection, photocatalysis, biomedical diagnostics, and industrial process monitoring.^[9,15–18]

Based on these theoretical advantages, the design and fabrication of real TP structures for practical applications have been studied. Recent approaches utilizing cavity-layer coupling, additional layers such as metasurfaces,^[19] topological insulators,^[20] and two-dimensional (2D) materials, including graphene and transition metal dichalcogenides,^[21–24] have enhanced the available TP modes through adjustment of additional coupling. However, although these attempts successfully enhanced the resonator performance, they diminished the manufacturing advantages of the TP and planar structure. From the design point of view for satisfying both performance and manufacturing issues, DBR layers were stacked onto the metal reflector as a reversed structure from conventional TP structure. With reduced pairs of periodic layers (N) and by matching the impedance (Z) between

1. Introduction


Creating strongly coupled narrow absorption in the near infrared region is a critical requisite for investigating highly

S. H. Kim, J. H. Ko, Y. J. Yoo, M. S. Kim, Y. M. Song
School of Electrical Engineering and Computer Science
Gwangju Institute of Science and Technology
Gwangju 61005, Republic of Korea
E-mail: ymsong@gist.ac.kr

G. J. Lee
Department of Electronics Engineering
Pusan National University
Busan 46241, Republic of Korea

S. Ishii
International Center for Materials Nanoarchitectonics
National Institute of Materials Science (NIMS)
1-1 Namiki, Tsukuba, Ibaraki 305-0044, Japan

S. Ishii
Japan Science and Technology Agency
PRESTO
4-1-8 Honcho, Kawaguchi, Saitama 332-0012, Japan

 The ORCID identification number(s) for the author(s) of this article can be found under <https://doi.org/10.1002/adom.202102388>.

DOI: 10.1002/adom.202102388

DBR and metal layer, they represented higher Q factor and thinner configuration than conventional case.^[25–27] Nevertheless, the material selection limitation and the fact that N is tunable within an only integer range make perfect matching of Z difficult. Further, owing to the residual parasitic absorption that occurs in dielectric materials, increased N reduces the radiative loss and increases the nonradiative loss.^[27–29]

In recent decades, the discrepancy between ideal design and realistic fabrication has remained a challenge for thin-film and multilayer photonics. Various strategies have been introduced to overcome this problem, including the use of nanopatterning or colloidal mixtures with optical trapping below the target wavelength range.^[30,31] In most cases, the desired optical properties are realized by adjusting the porosities of the employed media,^[32] which are prepared using different methods, based on the effective medium theory.^[33] For practical implementation, several methods allowing precise, easy, and simultaneous control of the material porosity (P_r) and thickness to target values matching the pre-designed optical model have been successfully demonstrated.^[32] However, although porous TP structures (including mesoporous multilayer structures) have been reported for narrow-band absorber and sensor applications, an ideal design with a high Q-factor, featuring small N , and design scalability has not yet been achieved.

Here, we present a design flow for sub-micron planar TPs based on a single material, to achieve near-unity absorptance through Z matching, which is achieved by tailoring the refractive indices using P_r tuning in near infrared range. For structural optimization, we suggest a computational model with a consistent relation that modifies N and the refractive indices. As numerical confirmation, rigorous coupled-wave analysis (RCWA) is performed by sweeping over diverse material indices and structural configurations. The Q-factor, absorptance, and t_{opt} results are considered in the figure of merit (FOM), which is used as the TP performance evaluation index. Hence, we successfully design TPs with high absorptance ($\approx 99\%$) and Q-factors (≈ 45) in the Tamm state with two pairs of DBRs ($\approx 0.7 \mu\text{m}$) and composed of a single material. The required P_r is achieved using glancing angle deposition (GLAD), through which a porous area is applied between the nanocolumns.^[34] As a demonstration, single-material TPs (SMTPs) are combined with a metal–semiconductor–metal (MSM) photodetector with a narrow spectral response. As the metallic film is replaced with an MSM structure, the hot electrons originating from the Tamm state are converted into an electrical signal. Furthermore, the proposed SMTP–MSM photodetector is fabricated in array form realizing large-area scalability and high throughput. Empowered by the suggested design flows, our structure facilitates the realization of scalable, cost-effective SMTP and SMTP–MSM photodetectors for numerous applications demanding high-performance TPs.

2. Results and Discussion

2.1. Basic Concept of Single-Material Tamm Plasmons

Figure 1a is a schematic of a TP composed of a single-material DBR and MSM photodetector with an electric field profile (red line), showing strong confinement at the DBR/MSM interface.

As a representative example, we demonstrate these concepts using a combination of germanium (Ge) as the DBR layer and gold (Au) as the metal reflector. Figure 1b, inset, shows the refractive index (n) control method achieved by tuning P_r as the design strategy for single-material TPs (SMTPs). As shown in the schematic close view (Figure 1c), the $n_{\text{high}}/n_{\text{low}}$ layers (where n_{high} and n_{low} are the high and low refractive indexes, respectively) were composed of amorphous-Ge (a-Ge) and porous-Ge (P_r -Ge) media to modulate the effective refractive index (n_{eff}).^[34] Figure 1d shows a-Ge and P_r -Ge layers experimentally fabricated using GLAD, having vertical and slanted columnar shapes. The slanted columns were formed by tilting the substrate with respect to the incoming-vapor direction at the deposition angle. In accordance with the substrate tilt angle and owing to the atomic shadowing effect that arises during GLAD, the medium P_r was increased and, hence, n_{eff} was reduced.^[35] Figure 1e shows the calculated n_{eff} and extinction coefficient (k) distributions for different P_r ; k was zero for a near-infrared (NIR) range exceeding $1.5 \mu\text{m}$.

To compare the SMTPs with conventional Tamm resonators, we defined an FOM incorporating the Q-factor, absorptance, and t_{opt} of the structure. Note that t_{opt} was expressed as a relative value considering the resonant wavelength (λ_{res}) in the Tamm state (Figure S1 and Table S1, see Supporting Information). These parameters were considered in order to evaluate the narrowband and unity-absorption behaviors on a thin scale. Based on the suggested relation, we compared the FOMs of the SMTPs (a-Ge/ P_r -Ge) and conventional Tamm resonators (TiO₂/SiO₂, a-Ge/SiO₂, and Si/SiO₂). As shown in Figure 1f, the SMTPs exhibited the largest FOM (≈ 100), whereas the conventional Tamm resonators had relatively small FOMs. Interestingly, because of the perfectly matched Z of the suggested structure, even the SMTPs with two DBR pairs ($N = 2$) exhibited similar performance to TiO₂/SiO₂ TPs with $N = 4$, as indicated by the absorptance spectra (Figure S2 and Table S2, see Supporting Information). Figure 1g shows the relative t_{opt} and FOMs of the SMTPs, conventional structures, and structures reported in the literature.^[29,36] The results show that the suggested SMTPs represented the highest FOM even on a thin scale of t_{opt} and more comparisons are represented in Table S1 with several conventional cases (see Supporting Information). The proposed SMTPs exhibited the highest FOMs even on a thin scale (i.e., for low t_{opt}). Figure 1h shows the simulated electric-field magnitude profiles and absorptance at the SMTP resonance wavelengths. The electric field profile reveals a standing-wave pattern in the a-Ge/ P_r -Ge Tamm plasmon structure with a maximum at the bottom a-Ge/ P_r -Ge interface and a decay towards both the Au film and top of the structure. Note that the strong absorption at the interface between the metal and DBR indicates strong absorption in the Tamm state. Finally, Figure 1i shows near-unity absorption ($\approx 99\%$) and a remarkably high spectral resolution. In the contours of Figure 1S, each identified area enclosed by a white dash line represents the FOM over 80, which is difficult to realize by combining conventional materials (Table S1, see Supporting Information). As represented in Figure S1, a high value of FOM (>80) can be implemented at $N = 2$ and/or higher (see Supporting Information). Consequently, to implement a compact and high-performance TPs, we experimentally demonstrated with the configuration of $N = 2$.

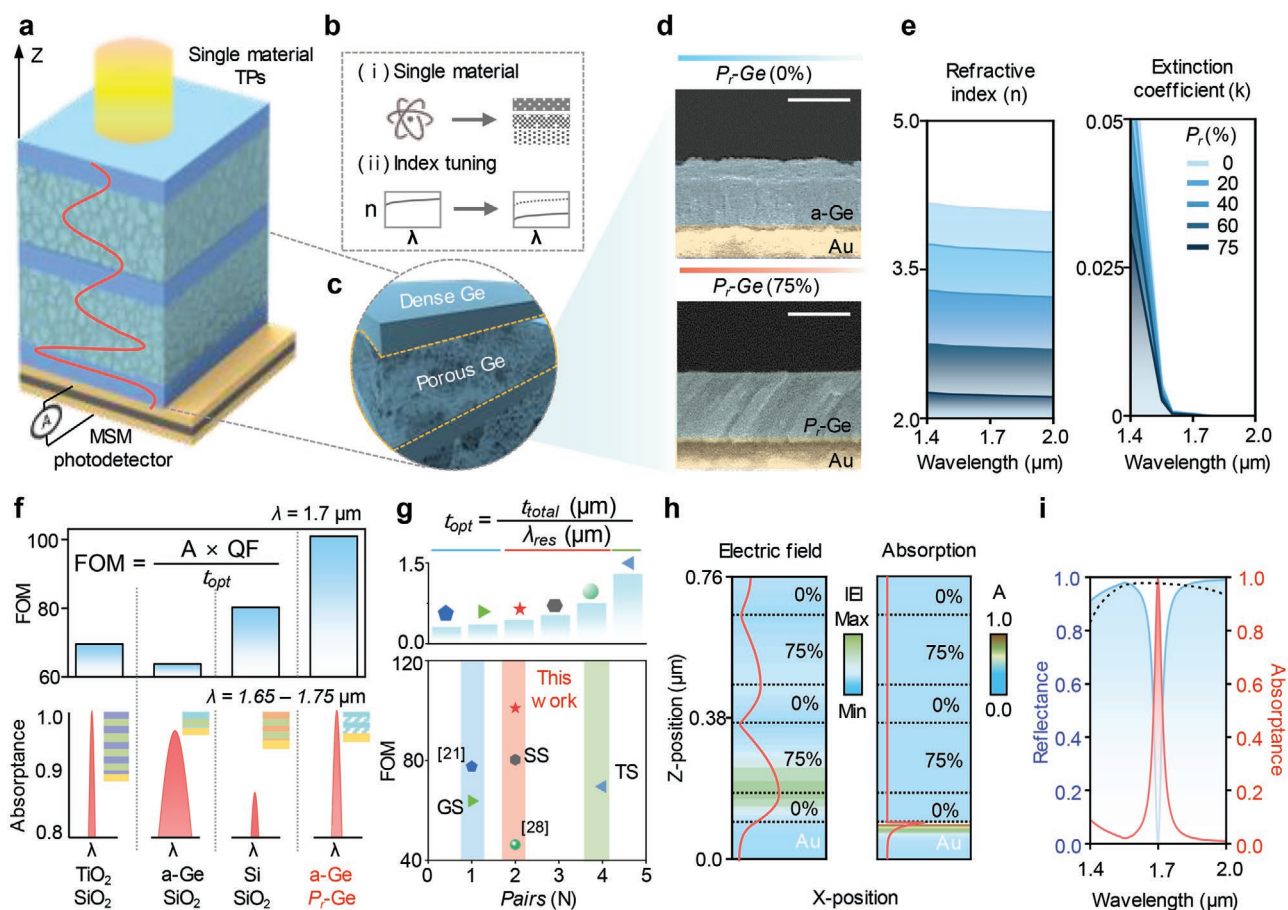


Figure 1. a) Schematic of single-material Tamm plasmons (SMTPs) composed of metal–semiconductor–metal (MSM) reflector and DBR structure. The red line represents the electric field profile. b) Schematic strategy for index tuning with a single material. c) Close view of dense amorphous Ge (a-Ge) and porous (P-Ge) structure of TP DBR layer. d) SEM images of a-Ge (upper) and P-Ge (lower). Scale bar: 100 nm. e) Refractive index (n) and extinction coefficient (k) corresponding to P_r change. f) Figures of merit (FOMs) and absorbance spectra of conventional structures (TiO₂/SiO₂, a-Ge/SiO₂, and Si/SiO₂) and SMTP obtained from simulation results. g) Comparison of the relative optical thickness (t_{opt}) and FOM with those of previously reported structures (TS, GS, and SS: TiO₂/SiO₂, a-Ge/SiO₂, and Si/SiO₂, respectively). h) SMTP. Each fraction represents a P_r of Ge. The red lines represent the electric field and absorption profile. i) Simulated absorbance and reflectance spectra of SMTP.

2.2. Optical Optimization Process for Porous Tamm Resonator

As a cornerstone to achieving narrowband and unity absorption, we optimized the Z of SMTPs and geometrical elements via a two-step process. First, an equivalent conjugate-matching circuit was established to tune the surface Z between the bottom surface of the DBR and the Au reflector, as depicted by Design Flow I in Figure 2a (upper). Second, to confirm the matched Z with respect to the structure absorbance and thickness, the configuration was engineered with varying thicknesses and by sweeping over the refractive indices of the DBR layers (n_{low} , n_{high}), as shown in Design Flow II, Figure 2a (lower). Figure 2b shows the calculated real and imaginary parts of the optical impedances Z_{Au} and Z_{DBR} for the p-polarized incident light. The imaginary Z components had opposite values, whereas the real components had the same value, at the Tamm-state resonance wavelength. This conjugated matching condition corresponded to an optical Tamm state at the DBR/Au interface, which yielded unity absorption.^[27] The Z calculation was confirmed for conventional materials, and the designed structure

was confirmed again by admittance loci plots that accurately approached (1,0), corresponding to perfect absorption (Figures S3 and S4, Supporting Information).^[37] To confirm the optical behavior of the designed SMTP structure, Figure 2c shows the calculated absorbance spectra for different last-layer thicknesses (t_{last}); the results correspond to different orders of the TP mode (Figure S5, see Supporting Information). The dashed horizontal lines in the contours correspond to the first-, second-, and third-order TP modes (i.e., $t_{last} = 78$, 283, and 487 nm, respectively). In this setup, each order of resonant conditions provided bandwidth tunability without alteration of the DBR layer structure (Figure S5, see Supporting Information). As indicated by the absorbance spectra, the three orders had the same absorbance ($\approx 99\%$) at the same λ with a narrow bandwidth. As Ge is almost transparent in the NIR range, the incident light could transmit through the DBR and interact with the DBR/Au interface without absorption, responding to changes in t_{last} . To confirm the dependency of the radiative/non-radiative losses on N, which has a decisive influence on Z, we varied N to 1, 2, and 4 pairs (Figure 2d). The standing-wave

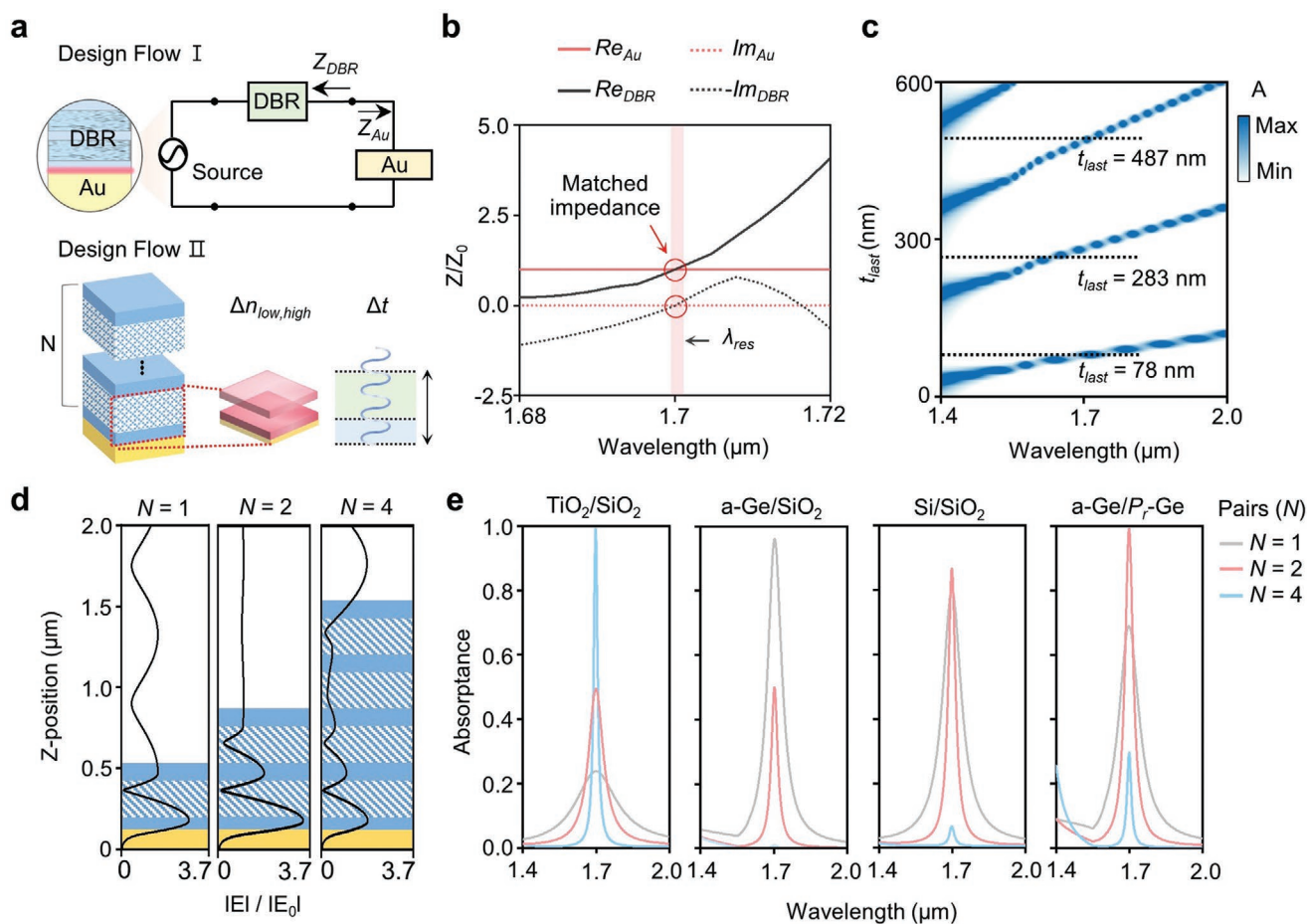


Figure 2. a) Design Flows I and II showing equivalent conjugate-matching circuit and numerical structure analysis process, respectively. b) Optical impedances (Z/Z_0) as functions of SMTP wavelength (Re and Im indicate real and imaginary components, respectively). c) Simulated absorbance contours for varying last-layer thickness (t_{last}). d) Profile of normalized electric field $|E|/|E_0|$ along z -axis with varying number of pairs (N). e) Simulated absorbance spectra for conventional TPs (TiO_2/SiO_2 , $a-Ge/SiO_2$, and Si/SiO_2) and SMTPs with $N = 1, 2$, and 4 .

patterns for the electric field indicate that the highest electric-field confinement was obtained near the Au layer for $N = 2$.

To extend our approach to the conventional materials (TiO_2/SiO_2 , $a-Ge/SiO_2$, Si/SiO_2), we calculated Z and simulated the absorbance spectra for each structure. Figure 2e shows simulated absorbance spectra for different N of 1, 2, and 4 for each structure. An optimal condition was apparent for each of the structures, i.e., $N = 4, 1, 2$, and 2 for TiO_2/SiO_2 , $a-Ge/SiO_2$, Si/SiO_2 , and $a-Ge/P_r-Ge$, respectively. Interestingly, no configuration for unity absorption with changing N was obtained for the $a-Ge/SiO_2$ and Si/SiO_2 combinations. These results are originated from the limitation regarding material selection and the fact that N is tunable within an integer range only, which indicates that there is an optimal combination of refractive indices for each configuration (i.e., N). This design rule is discussed in the next section.

2.3. Numerical Comparison for Each Configuration

To optimize the DBR-layer n (n_{low} , n_{high}) combination in the TP structure, we employed a computational model of the DBR

layer (n_{low} , n_{high}) with different N (1, 2, 3, and 4) on the metal reflector, in which the t_{opt} tailoring design rules for the DBR layer and t_{last} were incorporated (Supplementary Note 1, see Supporting Information). Figure 3a shows the absorbance and thickness contours obtained for varied n_{low} and n_{high} . In Figure 3b, the optimized areas with the desired absorbance (brown color, absorbance > 95%) and thickness (blue area, thickness < 800 nm) conditions (enclosed by the dashed lines in Figure 3a) are projected onto 2D space.

The optimized absorbance area narrowed and moved to the center diagonal line with increasing N , indicating a gradual decrease in the difference between n_{low} and n_{high} . This tendency originated from the intensity of the radiative/non-radiative loss given by the DBR layer.^[27] Accordingly, the optimized area of thickness is gradually narrowed with increasing N . To extend our approach to universal materials, we plotted the results for the structures with conventional n combinations (TiO_2/SiO_2 , $a-Ge/SiO_2$, Si/SiO_2) onto 2D space maps in Figure 3b. As indicated, implementation of unity absorption using these conventional materials was difficult, with the exception of TiO_2/SiO_2 with $N = 4$. This configuration yielded excellent absorbance and a narrow band; however, the use of high N yields thick devices.^[32,36]

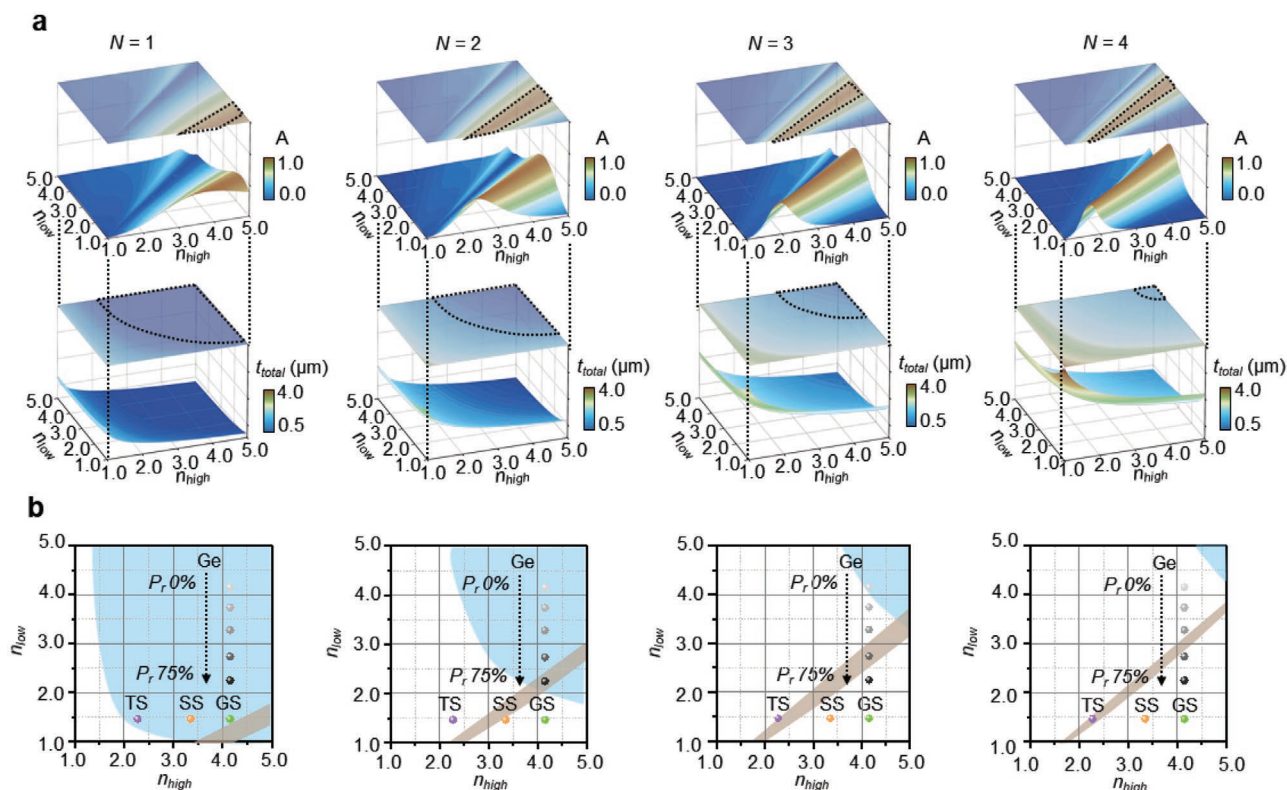


Figure 3. a) Absorbance and thickness contours corresponding to n sweeping for n_{low} and n_{high} layers with different N . b) Two-dimensional expression of optimized area. The area enclosed by the dashed line in (a) indicates the thickness range (0–800 nm) and absorbance scale (95–100%) for the given N .

Strategically, we customized the n_{eff} of the high-index material (Ge) by tuning P_r from 0–75%, as represented by absorption profiles in Figures S10 and Table S3 (see Supporting Information). For Ge, the combination of a-Ge/ P_r -75% with $N = 2$ was optimal in terms of absorbance and thickness. When this configuration was applied to the designed structure through Z matching, the Tamm state was satisfied. On the other hand, by considering the combination of refractive index with conventional materials, the spectral analysis has proceeded with n_{high} material (Si), and n_{low} material (TiO_2 and Si_3N_4), which have similar refractive index of a-Ge/ P_r -Ge, respectively. As a result, in the configuration of $N = 2$, they show significantly low absorption. These results can be explained with Figure 3b, Figure S11, and Table S4 (see Supporting Information). As described in Figure S11, the refractive index combination of n_{high} , n_{low} of the suggested conventional material is placed in optimized area for $N = 3$. Consequently, they should demand a larger N thick device which has over 1 μm . Finally, we identified the optimal configuration, i.e., Au/a-Ge/ P_r -Ge/a-Ge/ P_r -Ge/a-Ge with thicknesses of 50, 78, 187, 102.3, 187, and 102.3 nm, respectively (Supplementary Note 1, see Supporting Information). Additionally, for the universal application of the suggested concept, the calculation of SMTP of dense-/porous-layer with conventional materials (i.e., TiO_2 , Si) was performed. As discussed, by matching the combination of refractive index and N into optimized area, the absorbance spectra showed unity absorption, which represents well agreement with the result of Figure 3b. (Figure S12 and Table S5, see Supporting

Information). Furthermore, the angular dependency with varying polarization was compared, which shows less dispersive properties under s-polarization, otherwise p-polarization light affects typically more dispersive (Figure S13, Supporting Information).^[13,25,38] As exhibited in Figure S14 designed structure shows great angular dependency even under p-polarized light, which offers a promising applicability as a photodetection device (see Supporting Information). The angle insensitive performance could be explained by the fact that phase shift accumulated during the propagation through the DBR layers is relatively insignificant due to the small optical thickness of the DBR layers which originated from the high refractive indices of a-Ge/ P_r -75%.^[39]

2.4. Fabrication of Porous Tamm Resonator

To experimentally realize the designed TP structure, we modulated P_r by applying nanopores using GLAD. As depicted in Figure 4a, we tilted the deposition angle (DA) from 0° to 70° . Unidirectional slanted nanocolumns were formed by atomic shadowing depending on DA, with wider voids forming between the columns as DA increased. The n_{eff} variation arose from the P_r changes in the nanocolumns. Figure 4b shows the measured n_{eff} of fabricated structures with DAs of 0° and 70° , which yielded P_r values of 0% and 75%, respectively (Figure S15, see Supporting Information). As apparent from the cross-sectional SEM image (Figure 4c), alternating a-Ge and P_r -Ge

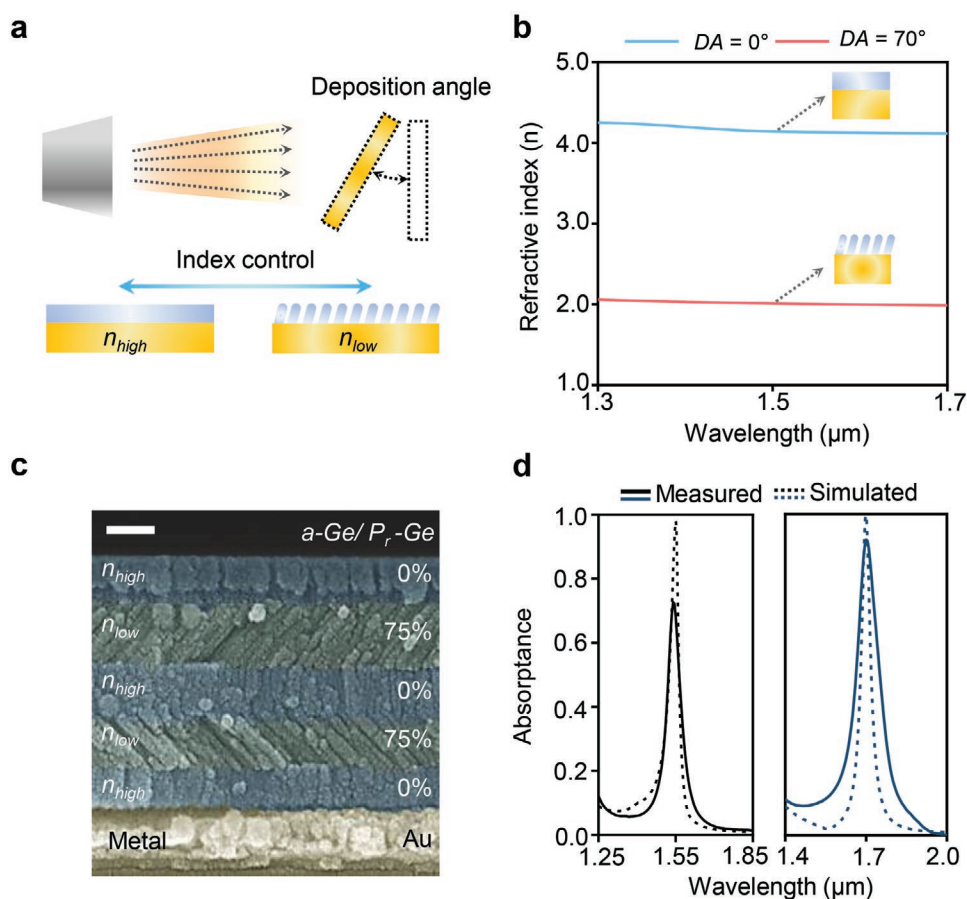


Figure 4. a) Schematic of glancing angle deposition (GLAD) process, where n_{eff} is controlled through deposition angle (DA) tilting. b) Measured n of Ge layers deposited with $DA = 0^\circ$ and 70° . c) Cross-sectional SEM image of optimized SMTP produced via a GLAD process. Scale bar: 100 nm. d) Comparison of measured (solid line) and simulated (dashed line) absorbance spectra for SMTPs having Tamm states at wavelengths $\lambda = 1.55 \mu\text{m}$ (black) and $1.7 \mu\text{m}$ (blue).

layers were deposited on the Au reflector. Figure 4d shows the measured (solid line) and simulated (dashed line) absorbance spectra for SMTPs having Tamm states at $\lambda = 1.55$ and $1.7 \mu\text{m}$ (black and blue plots, respectively). As revealed by the spectra, the resonant positions matched the simulation results well. The slight difference between experiment and simulation is likely due to differences in the actual and ideal optical properties of the materials.

2.5. Tamm resonator with photodetector

As a practical demonstration of a narrowband selective absorber, we fabricated a hot-electron photodetector that comprised an Au/Ti/ZnO/Ti/Au structure (i.e., MSM structure) and $a\text{-Ge}/P_r\text{-Ge}$ DBR layers. As shown in Figure 5a, the SMTP–MSM photodetector was realized through alternating deposition of a patterned MSM layer as the contact electrode (source and drain), with the top TP layer acting as a narrowband selective filter (Figure S16, see Supporting Information). The inset of Figure 5a represents the localized electric field at the interface between Au and the DBR layer, which indicates Tamm plasmon mode. To efficiently detect

the source light, we designed the SMTP–MSM structure such that hot electrons were generated at the MSM structure interface with unity absorption at the target λ (Figure S17, see Supporting Information). The designed structure had an Au/Ti/ZnO/Ti/Au/ $a\text{-Ge}/P_r\text{-Ge}/a\text{-Ge}/P_r\text{-Ge}/a\text{-Ge}$ configuration with thicknesses of 50, 2, 10, 2, 20, 73.5, 183, 99.1, 183, and 99.1 nm, respectively. Figure 5b shows the simulated absorption profile which shows strongly confined absorption magnitude superimposed on the real configuration at the MSM surface, which represents the strongly localized photons in the Au layer. To evaluate the SMTP–MSM device, the current-voltage (I – V) characteristics under dark conditions were measured, as shown in Figure 5c; the I – V curve indicates ohmic junction formation. A logarithmic scale I – V curve is shown in the inset of Figure 5c, revealing a dark current at zero bias of the order of 50 pA. The detailed energy state of the MSM is described by the band diagram shown in Figure 5d, where the Fermi level (E_F) is indicated by the black dashed line. The red dashed lines in the ZnO layer represent the conduction and valence band edges. From the literature, the energy barriers for electrons (ϕ_e) at the Ti/ZnO interface had a low value of less than 0.35 eV, which was based on the Ti work function (4.33 eV) and the electron

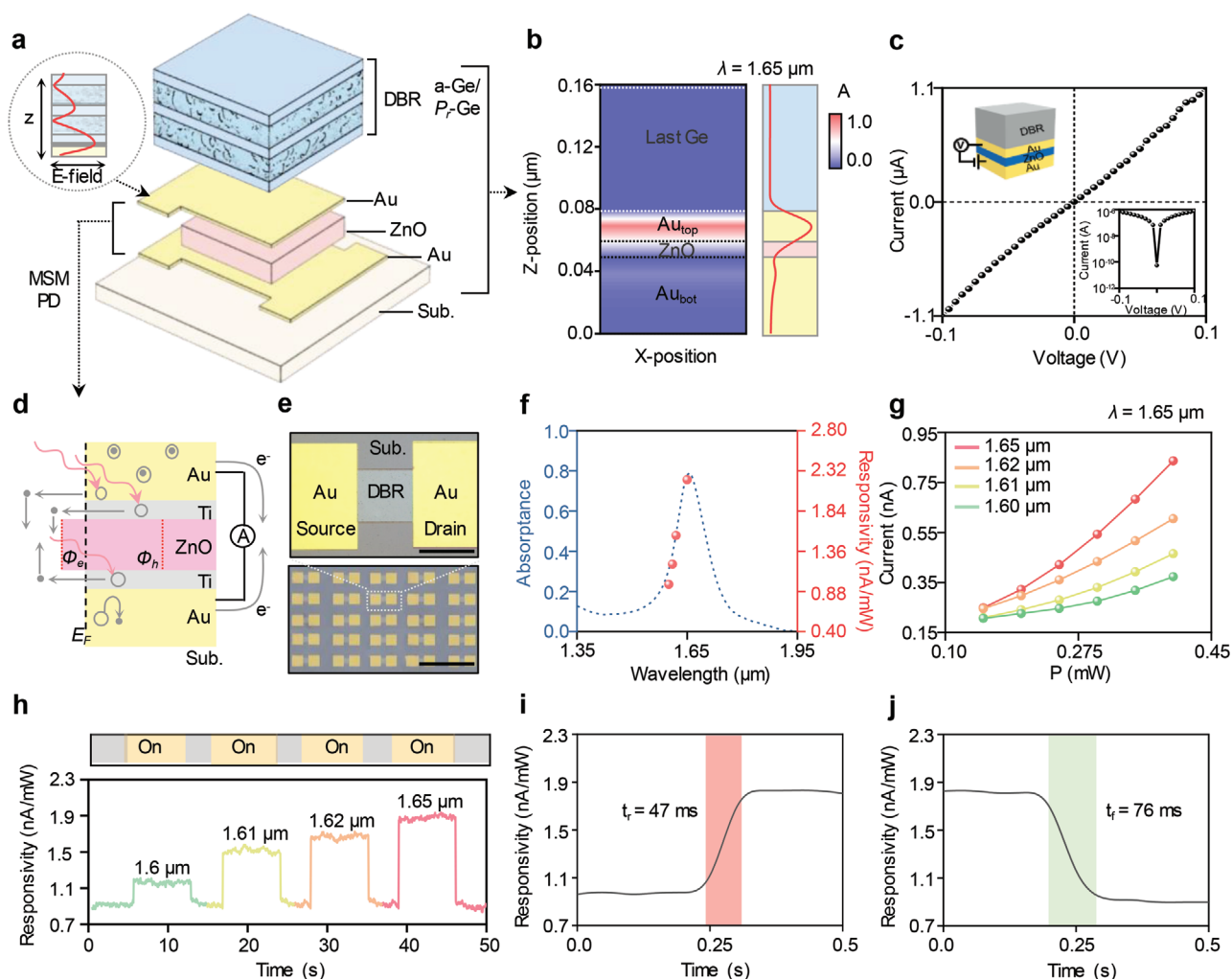


Figure 5. a) Schematic showing conjugation of SMTP and metal–semiconductor–metal (MSM) photodetector (PD). Inset represents the schematic of SMTP-MSM photodetector with electric field profile. b) Simulated absorption contours of SMTP-MSM structure (left) and absorption profile (red line) superimposed onto a position of real configuration (right). c) Measured current–voltage (I – V) curve of SMTP-MSM photodetector. Logarithmic-scale I – V curve (inset). d) Energy band diagram of SMTP-MSM photodetector. e) Optical microscopic image of fabricated SMTP-MSM structure (upper, scale bar: 500 μm) and photograph of SMTP-MSM array (lower, scale bar: 5 mm). f) Measured absorbance spectrum and photoresponsivity according to wavelength. g) Measured photocurrent corresponding to light-source power (P) for various spectral filters. h) Measured time-dependent photocurrent of SMTP-MSM photodetector without bias. Time-dependent photocurrents for i) rising and j) falling times.

affinity of ZnO (4.20–4.50 eV).^[40–42] This lowered energy barrier increased the probability of hot electrons passing through the interface. Furthermore, the inelastic collisions due to the ultra-thin thickness of ZnO layer than the mean free path (≈ 70 nm at 1 eV), enable small loss of 50% of electrons, during traversing the oxide.^[43–45] In a similar way, to improve the hot-electron lifetime, the thicknesses of the top Ti and Au layers were set to 2 and 20 nm, respectively, which is smaller than the electron mean free path.^[11,46] Using this structure, we fabricated an SMTP-MSM five-by-five array, as depicted in Figure 5e.

To quantitatively evaluate the SMTP-MSM, we experimentally measured the electronic properties by tuning the illumination λ using a customized setup (Figure S18, see Supporting Information). As shown in Figure 5f, the tendency of the electrical photoresponse for various incident λ

values at zero bias matched the measured absorbance spectrum well. Furthermore, the photocurrent was measured for monochromatic illumination with a different λ at zero bias (Figure 5g). The results show that the photocurrent increased close to the Tamm state ($\lambda = 1650$ nm). Further, the photocurrent linearity as a function of the incident light power (P) indicates a single-photon hot carrier.^[47] To evaluate the time-dependent photoresponse property, the SMTP-MDM photocurrent with time was determined for $\lambda = 1600$, 1610, 1620, and 1650 nm at zero bias, as shown in Figure 5h. The illumination was controlled by an optical shutter with a 7 s exposure time, and the results clearly displayed a rapid and stable response to the illuminating light. Moreover, to quantitatively confirm responsiveness, the rise, and fall times were measured, to be 47 and 76 ms, respectively (Figures 5i and j, respectively), for illuminating light with $\lambda = 1650$ nm.

3. Conclusion

We presented an effective strategy for the compact design of TP structures with a high Q-factor and unity absorptivity, in which a tunable effective-medium layer with geometrical simplicity and a sub-micron structure in the NIR range is employed. Our computational model indicated near-unity absorption ($\approx 99\%$) and a high Q-factor (≈ 45) with only two DBR pairs. Even for a few DBR pairs, the proposed structure exhibited superior performance to TPs consisting of many DBR pairs with great angular dependency. As a demonstration, an SMTP–MSM photodetector was developed through Z matching between the DBR and MSM to maximize the hot-electron concentration. The ohmic behavior of the MSM photodetector enhanced the response time and reversibility.

Such a single-material-based Tamm plasmonic structure and the design strategy could enhance the performance of photodetection devices as well as simplify the structures to miniaturize the overall device thickness. Owing to limitations concerning material selection, the ability to tailor the n_{eff} of the alternating optical structure shown in this study will facilitate the development of promising converging technologies for ultra-sensitive photodetectors with narrow and strong absorption. In addition, we expect that our design flow, through which the value of $n_{\text{high}}/n_{\text{low}}$ is customized for perfect Z matching, will constitute an effective and powerful means of achieving various 1D photonic structures. The combination of SMTPs with such high refractive index materials and tuning method of porosity would be helpful for demonstrating the devices on a thin scale demanding high-performance TPs such as photodetection, biomedical diagnostics, and industrial process monitoring.

4. Experimental Section

Optical Calculation: Calculations for the computational model were conducted using commercial software (DiffractionMOD, RSoft Design Group, USA) and the RCWA method to determine the reflectance and absorbance behaviors of the SMTPs and SMTP–MSM structure.^[48] The n and k values were obtained from the literature and from measured results (Figures S19 and S20, see Supporting Information).^[49–51] In the conventional structure, the diffraction was considered up to second order and a 0.2 nm grid size was used to calculate the diffraction efficiency. Because of the planar structures of the TPs, the above values were sufficient to numerically stabilize the results. The material dispersions and k values corresponding to the NIR range were considered to obtain exact outputs. MATLAB (Mathworks, Inc.), a commercial software package, was used to calculate the structural design parameter (t_{last} and the optical thickness of the last DBR layer). The detailed process of optical calculation using a computational model is explained with the calculation of spectral analysis with changing the structural parameters, effective refractive index, and impedance of SMTPs in Notes 1, 2, and 3 (see Supporting Information). Here, n_{eff} was calculated using MATLAB based on volume averaging theory.^[33]

Optical Characterization: The absorption spectra of the fabricated structure were measured using a UV–Vis–NIR spectrometer (LAMBDA 950, Perkin Elmer, USA) at a normal angle of incidence with a tungsten-halogen lamp as the source. The optical constants of the a-Ge and P_r -Ge were obtained using a dual rotating compensator ellipsometer (RC2, J.A. Woollam Co., Inc., USA) with a He-Ne laser as the source.

Fabrication of SMTP Structure: The thin-film layers of the suggested SMTPs were fabricated using an electron beam evaporator (KVE-E2000,

Korea Vacuum Tech, Ltd., Korea) under high vacuum ($\approx 10^{-6}$ Torr). The effective medium layers in the SMTPs were deposited by GLAD using customized sample holder, which has a tilted deposition angle (70°) to achieve porous-medium. For preparation, single-sided polished silicon (100) wafers were treated with a buffered oxide etchant for 3 min to remove the native oxide layer. Then, the wafers were sequentially sonicated for 5 min in acetone, methanol, and deionized water. The Au reflector was deposited at a rate of $\approx 2 \text{ \AA s}^{-1}$ to 50 nm thickness, which was sufficient to form a metal reflector (Figure S21, see Supporting Information). The a-Ge layer was deposited at a normal DA (0°). The P_r -Ge was deposited at a tilted angle (DA = 70°) to the target thickness at a rate of $\approx 1 \text{ \AA s}^{-1}$, following mounting of the substrate on an inclined sample holder (customized). To ensure uniformity, in our structure, each P_r -Ge layer of the first and second DBR pairs was deposited in the opposite direction (Figure S22, see Supporting Information).^[52]

Fabrication of SMTP–MSM Photodetector: To pattern the designed area (source and drain contact electrodes) photolithography was performed with an image reversal photoresist (AZ 5214, AZ Electronic Materials, Luxembourg). For the image reversal lithography process, a mask aligner (MJB3 UV400, Karl Suss, Germany) was used with a patterned chromium (Cr) photo mask. First, a 50 nm Au reflector was deposited on the patterned area to cover the area containing the source, active cell, and drain. Following lift-off, the Ti/ZnO/Ti/Au layers were sequentially deposited onto the area of the active cell and drain. The ZnO layer was deposited using a magnetron radio-frequency sputtering system (DDHT-LSH2, Daedong High Tech, Ltd., Korea) under a high vacuum ($\approx 10^{-6}$ Torr). This layer was deposited at 120°C , which yielded sufficient crystallinity (Figure S23 and Table S6, see Supporting Information). Finally, following additional lift-off, a-Ge/ P_r -Ge layers were alternately deposited onto the active cell area. Then, lift-off was performed to reveal each patterned area.

Photoresponse Measurement: The SMTP–MSM photodetector was characterized using a customized setup composed of a 300-W Xe lamp (Arc Lamp Housing 66902, Newport, USA) and optical components (Figure S18, see Supporting Information). The collimated source light was focused on the active area path through a prism mirror (MRA15-P01, Thorlabs, USA) and various bandpass filters (FB1600-12, FB1610-12, FB1620-12, FB1650-12; 1600, 1610, 1620, and 1650 nm, respectively; Thorlabs, USA).

Supporting Information

Supporting Information is available from the Wiley Online Library or from the author.

Acknowledgements

S.H.K. and J.H.K. contributed equally to this work. This work was supported by the GIST Research Institute (GRI) through a grant funded by the GIST and National Research Foundation of Korea (NRF) funded by the Ministry of Science and ICT (NRF-2021M3H4A1A04086552, NRF-2017M3D1A1039288). This work was also supported by the Institute of Information & Communications Technology Planning & Evaluation (IITP), through a grant funded by the Korean government (MSIT) (No.2020-0-01000). J.H.K. acknowledges the support from the NRF funded by the Ministry of Education (NRF-2021R1A6A3A13043651).

Conflict of Interest

The authors declare no conflict of interest.

Data Availability Statement

The data that support the findings of this study are available from the corresponding author upon reasonable request.

Keywords

photodetectors, porous nanocolumns, Tamm plasmons, unity absorption

Received: November 3, 2021

Revised: December 8, 2021

Published online: January 10, 2022

- [1] X. Zhou, W. Geng, J. Li, Y. Wang, J. Ding, Y. Wang, *Adv. Opt. Mater.* **2020**, *8*, 1902003.
- [2] M. Casalino, G. Coppola, M. Iodice, I. Rendina, L. Sirteto, *Sensors* **2010**, *10*, 10571.
- [3] J. Miao, W. Hu, N. Guo, Z. Lu, X. Zou, L. Liao, S. Shi, P. Chen, Z. Fan, J. C. Ho, *ACS Nano* **2014**, *8*, 3628.
- [4] C. Ng, L. Wesemann, E. Panchenko, J. Song, T. J. Davis, A. Roberts, D. E. Gómez, *Adv. Opt. Mater.* **2019**, *7*, 1801660.
- [5] J. Mejía-Salazar, O. N. Oliveira Jr, *Chem. Rev.* **2018**, *118*, 10617.
- [6] Y. K. Srivastava, M. Manjappa, H. N. Krishnamoorthy, R. Singh, *Adv. Opt. Mater.* **2016**, *4*, 1875.
- [7] A. E. Miroshnichenko, *Phys. Rev. E* **2009**, *79*, 026611.
- [8] B. Luk'yanchuk, N. I. Zheludev, S. A. Maier, N. J. Halas, P. Nordlander, H. Giessen, C. T. Chong, *Nat. Mater.* **2010**, *9*, 707.
- [9] B. Auguié, M. C. Fuertes, P. C. Angelomé, N. L. Abdala, G. J. Soler Illia, A. Fainstein, *ACS Photonics* **2014**, *1*, 775.
- [10] H. Reather, *Surface Plasmons on Smooth and Rough Surfaces and on Gratings*, Vol. 111, Springer-Verlag, Berlin **1983**.
- [11] C. Zhang, K. Wu, V. Giannini, X. Li, *ACS Nano* **2017**, *11*, 1719.
- [12] Z.-Y. Yang, S. Ishii, T. Yokoyama, T. D. Dao, M.-G. Sun, T. Nagao, K.-P. Chen, *Opt. Lett.* **2016**, *41*, 4453.
- [13] M. Kaliteevski, I. Iorsh, S. Brand, R. Abram, J. Chamberlain, A. Kavokin, I. Shelykh, *Phys. Rev. B* **2007**, *76*, 165415.
- [14] A. Kavokin, I. Shelykh, G. Malpuech, *Phys. Rev. B* **2005**, *72*, 233102.
- [15] Z. Wang, J. K. Clark, Y.-L. Ho, J.-J. Delaunay, *Nanoscale* **2019**, *11*, 17407.
- [16] J. Wang, Y. Zhu, W. Wang, Y. Li, R. Gao, P. Yu, H. Xu, Z. Wang, *Nanoscale* **2020**, *12*, 23945.
- [17] Y. Zhu, P. Yu, T. Liu, H. Xu, A. O. Govorov, Z. Wang, *ACS Appl. Electron. Mater.* **2020**, *3*, 639.
- [18] Z. Balevičius, *Coatings* **2020**, *10*, 1187.
- [19] O. Buchnev, A. Belosludtsev, V. Reshetnyak, D. R. Evans, V. A. Fedotov, *Nanophotonics* **2020**, *9*, 897.
- [20] H. Lu, Y. Li, Z. Yue, D. Mao, J. Zhao, *APL Photonics* **2019**, *4*, 040801.
- [21] K. Zhou, L. Lu, J. Song, B. Li, Q. Cheng, *J. Appl. Phys.* **2018**, *124*, 123102.
- [22] H. Lu, X. Gan, B. Jia, D. Mao, J. Zhao, *Opt. Lett.* **2016**, *41*, 4743.
- [23] J. Hu, Y. Huang, Y. Chen, J. Wu, J. Wang, *Opt. Mater. Express* **2021**, *11*, 3833.
- [24] H. Lu, X. Gan, D. Mao, Y. Fan, D. Yang, J. Zhao, *Opt. Express* **2017**, *25*, 21630.
- [25] M. He, J. R. Nolen, J. Nordlander, A. Cleri, N. S. McIlwaine, Y. Tang, G. Lu, T. G. Folland, B. A. Landman, J.-P. Maria, *Nat. Mater.* **2021**, *20*, 1663.
- [26] S. V. Boriskina, Y. Tsurimaki, *J. Phys.: Condens. Matter* **2018**, *30*, 224003.
- [27] Y. Tsurimaki, J. K. Tong, V. N. Boriskina, A. Semenov, M. I. Ayzatsky, Y. P. Machekhin, G. Chen, S. V. Boriskina, *ACS Photonics* **2018**, *5*, 929.
- [28] B. Auguié, A. Bruchhausen, A. Fainstein, *J. Opt.* **2015**, *17*, 035003.
- [29] Z.-Y. Yang, S. Ishii, T. Yokoyama, T. D. Dao, M.-G. Sun, P. S. Pankin, I. V. Timofeev, T. Nagao, K.-P. Chen, *ACS Photonics* **2017**, *4*, 2212.
- [30] L. Ferrier, H. S. Nguyen, C. Jamois, L. Berguiga, C. Symonds, J. Bellessa, T. Benyattou, *APL Photonics* **2019**, *4*, 106101.
- [31] M. Wurdack, N. Lundt, M. Klaas, V. Baumann, A. V. Kavokin, S. Höfling, C. Schneider, *Nat. Commun.* **2017**, *8*, 259.
- [32] A. Juneau-Fecteau, L. G. Fréchette, *Opt. Mater. Express* **2018**, *8*, 2774.
- [33] A. Garahan, L. Pilon, J. Yin, I. Saxena, *J. Appl. Phys.* **2007**, *101*, 014320.
- [34] N. G. Wakefield, J. B. Sorge, M. T. Taschuk, L. W. Bezuidenhout, M. J. Brett, J. C. Sit, *J. Opt. Soc. Am. A* **2011**, *28*, 1830.
- [35] R. N. Tait, T. Smy, M. J. Brett, *J. Vac. Sci. Technol., A* **1992**, *10*, 1518.
- [36] Z. Wang, J. K. Clark, Y.-L. Ho, B. Vilquin, H. Daiguji, J.-J. Delaunay, *Appl. Phys. Lett.* **2018**, *113*, 161104.
- [37] H. A. Macleod, *Thin-Film Optical Filter*, Institute of Physics, London, **2001**.
- [38] X. Liu, Z. Li, Z. Wen, M. Wu, J. Lu, X. Chen, X. Zhao, T. Wang, R. Ji, Y. Zhang, *Nanoscale* **2019**, *11*, 19742.
- [39] K.-T. Lee, C. Ji, L. J. Guo, *Appl. Phys. Lett.* **2016**, *108*, 031107.
- [40] H. B. Michaelson, *J. Appl. Phys.* **1977**, *48*, 4729.
- [41] H. Moormann, D. Kohl, G. Heiland, *Surf. Sci.* **1980**, *100*, 302.
- [42] K. Jacobi, G. Zwicker, A. Gutmann, *Surf. Sci.* **1984**, *141*, 109.
- [43] H. Chalabi, D. Schoen, M. L. Brongersma, *Nano Lett.* **2014**, *14*, 1374.
- [44] W. Krolkowski, W. Spicer, *Phys. Rev. B* **1970**, *1*, 478.
- [45] M. P. Seah, W. Dench, *Surf. Interface Anal.* **1979**, *1*, 2.
- [46] A. M. Brown, R. Sundararaman, P. Narang, W. A. Goddard III, H. A. Atwater, *ACS Nano* **2016**, *10*, 957.
- [47] T. Gong, J. N. Munday, *Nano Lett.* **2015**, *15*, 147.
- [48] M. Moharam, E. B. Grann, D. A. Pomet, T. Gaylord, *J. Opt. Soc. Am. A* **1995**, *12*, 1068.
- [49] D. T. Pierce, W. E. Spicer, *Phys. Rev. B* **1972**, *5*, 3017.
- [50] I. H. Malitson, *J. Opt. Soc. Am.* **1965**, *55*, 1205.
- [51] S. Ratzsch, E.-B. Kley, A. Tünnermann, A. Szeghalmi, *Nano-technology* **2014**, *26*, 024003.
- [52] J. Oliver, T. Kessler, C. Smith, B. Taylor, V. Gruschow, J. Hettrick, B. Charles, *Opt. Express* **2014**, *22*, 23883.